

Resolving the polarization of high-order harmonic generation by temporal multislit interferometrySen Qiao,¹ Liang Li,^{1,*} Xiaosong Zhu,¹ Pengfei Lan,^{1,†} and Peixiang Lu^{1,2,3}¹*School of Physics and Wuhan National Laboratory for Optoelectronics, Huazhong University of Science and Technology, Wuhan 430074, China*²*Hubei Key Laboratory of Optical Information and Pattern Recognition, Wuhan Institute of Technology, Wuhan 430205, China*³*CAS Center for Excellence in Ultra-intense Laser Science, Shanghai 201800, China*

(Received 8 June 2021; accepted 11 August 2021; published 30 August 2021)

We propose a temporal multislit interference model of high-order harmonic generation (HHG). By using the interference picture, we investigate the polarization features of harmonics generated by atoms and the two-dimensional synthesized driving laser fields. The result shows that the selection rules and ellipticity of harmonics can be understood by intracycle interference. Based on quantum path analysis, we show the harmonic polarization can be controlled by modifying the structure of the temporal interferometer. We perform a quantitative analysis of the harmonic polarization spectrum in terms of electron dynamics and provide an intuitive picture and a general tool for HHG investigation.

DOI: [10.1103/PhysRevA.104.023114](https://doi.org/10.1103/PhysRevA.104.023114)**I. INTRODUCTION**

High-order harmonic generation (HHG) is an extremely nonlinear phenomenon, which occurs in the interaction of intense femtosecond laser fields with atoms or molecules. It provides a convenient and popular approach for generating extreme ultraviolet or x-ray attosecond pulses [1–3]. Moreover, the abundant information in the high harmonic spectrum provides unique access to probe the structure and dynamics of targets [4–7]. The HHG process can be understood by the semiclassical three-step recollision (TSR) model [8–10]. The electron is first ionized and subsequently accelerated by the driving laser fields. When the direction of driving field reverses, the electron is pulled back and collides with the parent ion, thereby the high-energy photon is emitted. In linearly polarized driving fields, electrons return to the parent ions along the laser polarization direction; thereby harmonics generated by isotropy targets are linearly polarized. In comparison, circularly or elliptically polarized harmonics have more value in numerous applications, e.g., chiral recognition [11], the study of ultrafast chiral-specific dynamics [12], and x-ray magnetic circular dichroism spectroscopy [13].

In recent years, elliptically polarized attosecond pulses [14–20] have received a lot of attention. Several schemes were developed to produce harmonics with tunable ellipticity. One scheme is based on the use of prealigned molecules [21,22]. In this approach, however, the measured ellipticity can hardly exceed 0.35, and the control over polarization is difficult. Another scheme is realized by using two-dimensional (2D) driving fields. By employing elliptically polarized driving fields, harmonics can have nonzero ellipticity but poor yield

[23–25]. To solve this issue, the synthesized driving laser field scheme was proposed. A useful method is employing the bichromatic counterrotating circularly polarized (BCCP) driving laser fields [15,18,26–28]. When irradiating targets with BCCP fields, only specific harmonics can be effectively generated, which is known as the selection rule [29]. The allowed harmonics are purely circularly polarized, and the efficiency is comparable to that in the linearly polarized driving field. Moreover, the polarization of the harmonics can be fully controlled by adjusting the driver without compromising the efficiency. In recent works, another method was developed based on the orthogonal two-color (OTC) fields [30–34]. Symmetry arguments dictate that harmonics generated by OTC fields and isotropy targets are linearly polarized [35]. Nevertheless, when adjusting the cross angle between two drivers, the symmetry break leads to the generation of elliptically harmonics. It was shown that the harmonics generated by nearly OTC laser fields (i.e., the crossing angle is near 90°) can have large ellipticity. Additionally, the control over polarization is easy to realize with this method.

In order to realize optimal control, it is significant to figure out the mechanism of how the driving fields affect the harmonics. It is complicated to describe the ellipticity of harmonics within the framework of the TSR model. There are several other perspectives to understand the properties of harmonics. One method is based on the dynamical symmetry of the interaction system. The Floquet group theory successfully explains the selection rules and the polarization of allowed harmonics [36,37]. Another method is based on the conservation law in the HHG process [28,38]. Previous works showed the ellipticity of harmonics in BCCP fields can easily be explained by the spin angular momentum of absorbed photons [28]. However, it is inconvenient to extend these methods to other driving

*liangl@hust.edu.cn

†pengfeilan@hust.edu.cn

fields, especially the driving fields which do not have well-defined dynamical symmetry and spin angular momentum.

In this paper, we investigate the polarization of harmonics in the view of temporal multislit interferometry. First, we show its applications to explain the selection rules and polarization features in BCCP and OTC fields. Next, based on quantum path analysis, we investigate the origin of ellipticity in nearly OTC fields. The results demonstrate that the asymmetry of quantum paths, i.e., their dynamical phase, recollision time, and recombination directions determine the polarization of harmonics. Finally, we discuss the control over polarization from the perspective of temporal interference.

This paper is organized as follows. In Sec. II, we introduce our model and calculation method. The calculation and analysis results are presented in Sec. III. Finally, we conclude our study in Sec. IV.

II. THEORETICAL MODEL

A. Numerically solving the time-dependent Schrödinger equation

In order to verify our model, we calculated the harmonic spectrum by numerically solving the 2D time-dependent Schrödinger equation (TDSE) as a reference. The He atom is selected for its central symmetry. In the length gauge, the TDSE is given by [39]

$$i \frac{\partial \Psi(\mathbf{r}, t)}{\partial t} = \left[-\frac{1}{2} \nabla^2 + V(\mathbf{r}) + \mathbf{r} \cdot \mathbf{E} \right] \Psi(\mathbf{r}, t). \quad (1)$$

Atomic units are used throughout unless stated otherwise. Here $\Psi(\mathbf{r}, t)$ represents the wave function, and \mathbf{r} denotes the electron position. $V(\mathbf{r}) = -1/\sqrt{\mathbf{r}^2 + b}$ is the soft-core potential, and b is the soft-core parameter. The 2D laser field is written as

$$\mathbf{E} = f(t) \begin{bmatrix} E_x(t) \\ E_y(t) \end{bmatrix}. \quad (2)$$

The wavelength of the fundamental field is 800 nm. $f(t)$ is a trapezoidal envelope with three-cycle rising and three-cycle falling edges and an eight-cycle plateau. We use the split-operator method to solve Eq. (1), and the time-dependent dipole acceleration can be obtained with Ehrenfest's theorem:

$$\ddot{\mathbf{D}}(t) = -\langle \Psi(t) | H(t), [H(t), \mathbf{r}] | \Psi(t) \rangle. \quad (3)$$

Then, the harmonic spectrum can be calculated by Fourier transformation,

$$\mathbf{E}^{\text{hhg}}(\omega) = - \int \ddot{\mathbf{D}} \exp(-i\omega t) dt. \quad (4)$$

It can be decomposed into right- and left-circularly polarized components:

$$E_{\pm}^{\text{hhg}} = \frac{1}{\sqrt{2}} (E_x^{\text{hhg}} \pm iE_y^{\text{hhg}}). \quad (5)$$

The polarization state of the harmonics can be characterized by the degree of circular polarization (DCP) ζ [40]:

$$\zeta = \frac{I_+ - I_-}{I_+ + I_-}, \quad (6)$$

where $I_{\pm} = |E_{\pm}^{\text{hhg}}|^2$ denotes the intensity of the helical components. ζ is connected to the ellipticity ϵ [41],

$$\zeta = \frac{2\epsilon}{1 + \epsilon^2}, \quad (7)$$

and the sign of ζ indicates the helicity h of harmonics:

$$h = \text{sgn}(\epsilon) = \text{sgn}(\zeta). \quad (8)$$

B. Principle of temporal multislit interference

According to Feynman's path integral, any quantum mechanical process can be represented as a coherent superposition of contributions of all possible paths [42]. Therefore, as the left panel in Fig. 1 shows, the instantaneous dipole moment $\mathbf{D}(t)$ is contributed by all possible quantum paths [7],

$$\mathbf{D}(t) = \sum a_{\text{ion}}(\mathbf{k}', t') e^{iS(\mathbf{k}, t; \mathbf{k}', t')} \mathbf{a}_{\text{rec}}(\mathbf{k}, t), \quad (9)$$

where \mathbf{k}' and \mathbf{k} denote the initial and final mechanical momenta of each path. a_{ion} and \mathbf{a}_{rec} represent the amplitude of ionization and spontaneous recombination. Here $\exp(iS)$ is the propagation factor, which is the integral of the Lagrangian L :

$$S = \int_{t'}^t L dt, \quad L = \frac{\nabla^2}{2} - V(\mathbf{r}) - \mathbf{r} \cdot \mathbf{E}. \quad (10)$$

The harmonic spectrum can be calculated by Fourier transformation of $\mathbf{D}(t)$:

$$\begin{aligned} \mathbf{E}^{\text{hhg}}(\omega) &= \int \mathbf{D}(t) e^{-i\omega t} dt \\ &= \sum a_{\text{ion}}(\mathbf{k}', t') e^{i[S(\mathbf{k}, t; \mathbf{k}', t') - \omega t]} \mathbf{a}_{\text{rec}}(\mathbf{k}, t). \end{aligned} \quad (11)$$

Previous works showed that strong-field ionization is an intrinsic attosecond process, which mainly occurs around the instantaneous maximum of the driving field [43], and the emission in the time domain is a train of attosecond bursts [44,45]. Therefore, $\mathbf{D}(t)$ can be divided into several bursts,

$$\mathbf{D}(t) = \sum_j \mathbf{D}_j(t). \quad (12)$$

These bursts create a multislit in the time domain, and the HHG spectrum is the interference fringe in the frequency domain:

$$\mathbf{E}^{\text{hhg}}(\omega) = \int \sum_j \mathbf{D}_j(t) e^{-i\omega t} dt = \sum_j \mathbf{B}_j(\omega). \quad (13)$$

In the 2D driving field, the direction of $\mathbf{D}(t)$ rotates in the polarization plane of the driving field. Therefore, these $\mathbf{B}_j(\omega)$ have different polarizations. For harmonics with high energy, electrons recollide with the nucleus nearly straight on. As the ground state is isotropic, each $\mathbf{B}_j(\omega)$ can be simplified as a linearly polarized component. Then Eq. (13) can be rewritten as

$$\begin{aligned} \mathbf{E}^{\text{hhg}}(\omega) &= \sum_j \mathbf{C}_j(\omega) \exp i\varphi_j(\omega) \\ &= \sum_j |\mathbf{C}_j(\omega)| \begin{bmatrix} \cos \alpha_j(\omega) \\ \sin \alpha_j(\omega) \end{bmatrix} \exp[i\varphi_j(\omega)], \end{aligned} \quad (14)$$

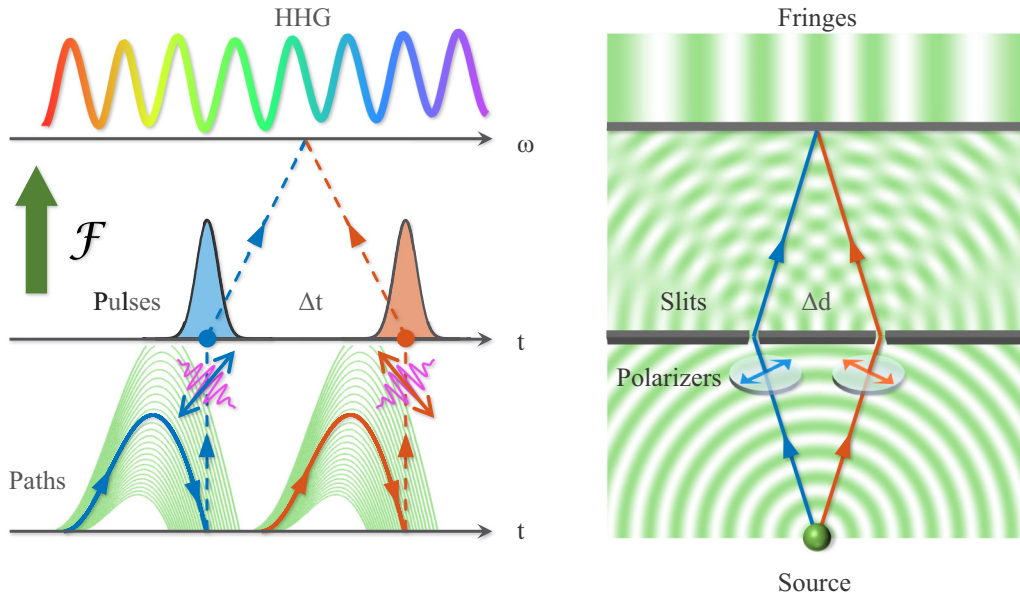


FIG. 1. The graph on the left shows the temporal interference model of HHG. From the bottom to the top, it shows the quantum paths, temporal emissions, and the harmonic spectrum. The blue and orange solid lines denote two representative quantum paths. The graph on the right shows the typical Young's double-slit interferometer.

where each \mathbf{C}_j is a vector. Its amplitude and polarization angle are $|\mathbf{C}_j|$ and α_j . Equation (14) is equivalent to Young's interferometer with polarizers, as shown in the right panel of Fig. 1. The right- and left-circularly polarized components of the harmonics can be written as

$$\mathbf{E}_{\pm}^{\text{hhg}}(\omega) = \sum_j \frac{|\mathbf{C}_j(\omega)|}{2} \begin{bmatrix} 1 \\ \mp i \end{bmatrix} \exp[i\{\varphi_j(\omega) \pm \alpha_j(\omega)\}]. \quad (15)$$

If the interaction system has specific dynamical symmetry, the above interference can easily be understood. Generally, the temporal interference can be calculated by quantum path analysis. Although HHGs are contributed by infinite paths, the temporal interference can be calculated by analyzing several representative paths. We consider only paths which satisfy the classical Lagrangian equation of motion. For the sake of simplicity, the effect of the Coulomb potential is neglected.

$$\mathbf{F} = \frac{d}{dt} \left(\frac{\partial L}{\partial \mathbf{k}} \right) - \frac{\partial L}{\partial \mathbf{r}} = \mathbf{E}. \quad (16)$$

According to the adiabatic approximation, the initial momentum of each electron is perpendicular to the instantaneous direction of the driving field. For harmonics with specific energy ω , we select only those trajectories whose return energy satisfies $I_p + |\mathbf{k}_r|^2/2 = \omega$, where I_p is the ionization energy. The interference in Eq. (14) can be calculated as follows.

The total amplitude $|\mathbf{C}|$ is related to the ionization and recollision amplitudes given by the scalar function $\Upsilon(\mathbf{k}_i)$ and the transition dipole matrix element $\mathbf{d}^*(\mathbf{k}_r)$ [46,47]:

$$|\mathbf{C}| \propto |\Upsilon(\mathbf{k}_i)\mathbf{d}^*(\mathbf{k}_r)| = \left| \left(I_p + \frac{\mathbf{k}_i^2}{2} \right) \langle \mathbf{k}_i | g \rangle \langle g | \mathbf{r} | \mathbf{k}_r \rangle \right|. \quad (17)$$

We ignore the ground-state depletion and apply the plane wave approximation. The polarization direction α is parallel to the direction of recollision momentum \mathbf{k}_r . The total phase φ

contains two parts. S is the phase related to electron dynamics:

$$\varphi = S - \omega t_r, \quad S = I_p(t_r - t_i) + \int_{t_i}^{t_r} \frac{|\mathbf{k}|^2}{2} dt. \quad (18)$$

III. RESULTS AND DISCUSSION

A. Polarization of harmonics in the BCCP and OTC driving fields

The BCCP driving field is obtained by combining the right-circularly polarized fundamental field and the left-circularly polarized second-harmonic (SH) field. The field can be written as

$$\mathbf{E}(t) = E_0 f(t) \begin{bmatrix} \cos(\omega_0 t) + \cos(2\omega_0 t) \\ \sin(\omega_0 t) - \sin(2\omega_0 t) \end{bmatrix}. \quad (19)$$

As Fig. 2(a) shows, the Lissajous figure of the driving field has threefold rotational symmetry. The $3n$ -order (n is a positive integer) harmonics are absent. The $(3n+1)$ -order and $(3n-1)$ -order harmonics are circularly polarized with the same helicity as the fundamental and SH fields, respectively. To analyze the temporal properties of harmonics, we employ the Gabor time-frequency analysis [48] in Fig. 2(b). There are three dominant channels in each optical cycle. The intracycle interference can be described as

$$\mathbf{E}^{\text{hhg}}(\omega) = \mathbf{C}_1 + \mathbf{C}_2 e^{\Delta\varphi} + \mathbf{C}_3 e^{2\Delta\varphi}, \quad \Delta\varphi = \omega\Delta t = \frac{\omega}{\omega_0} \frac{2\pi}{3}, \quad (20)$$

where \mathbf{C}_1 , \mathbf{C}_2 , and \mathbf{C}_3 are three vectors shown in Fig. 2(c). Their angle difference is $2\pi/3$. Their time delay leads to the phase difference $\Delta\varphi$. Consequently, as shown in Fig. 2(d), the temporal interference of $3n$ -order harmonics can be simplified as $\mathbf{C}_1 + \mathbf{C}_2 + \mathbf{C}_3 = \mathbf{0}$, which is completely destructive. As a result, $3n$ -order harmonics are suppressed. To investigate the ellipticity features of $(3n \pm 1)$ -order harmonics, we focus on

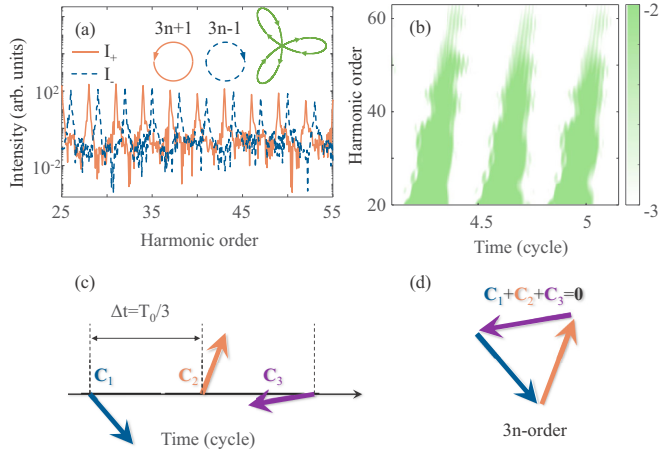


FIG. 2. The calculation results in the BCCP field. The intensity of the fundamental and SH fields is 5×10^{14} W/cm². (a) The intensity of helical components of harmonics. (b) The time-frequency spectrogram of the HHG. The color map represents the intensity distribution in the logarithmic scale. (c) The schematic diagram of intracycle interference. The three arrows show the amplitude, polarization angle, and emission time of three temporal components. (d) The interference result of $3n$ -order harmonics.

interference of each helical harmonic component. The right- and left-circularly polarized components of the harmonics can be represented as

$$\mathbf{E}_{\pm}^{\text{hhg}}(\omega) \propto \sum_{j=1}^3 \left[\frac{1}{\mp i} \right] \exp \left\{ -i \left[j \frac{2\pi}{3} \left(\frac{\omega}{\omega_0} \mp 1 \right) \right] \right\}. \quad (21)$$

The right- and left-circularly polarized harmonics can be coherently enhanced when

$$\frac{2\pi}{3} \left(\frac{\omega}{\omega_0} \mp 1 \right) = 2n\pi, \quad \frac{\omega}{\omega_0} = 3n \pm 1. \quad (22)$$

Therefore, $(3n + 1)$ -order harmonics are purely right circularly polarized, and $(3n - 1)$ -order harmonics are purely left circularly polarized, which is coincident with the selection rules.

Next, we use the same method to analyze the harmonics in the OTC field. The fundamental field is along the x axis, and the SH field is along the y axis. The relative phase between them is fixed to $\pi/2$. The OTC field is represented as

$$\mathbf{E}(t) = E_0 f(t) \begin{bmatrix} \cos(\omega_0 t) \\ \cos(2\omega_0 t - \pi/2) \end{bmatrix}. \quad (23)$$

As Fig. 3(a) shows, the Lissajous figure of the driving field is symmetric about the y direction. Odd- and even-order harmonics are linearly polarized in the same direction as the fundamental and SH fields, respectively. The time-frequency spectrogram in Fig. 3(b) shows there are two dominant channels in each optical cycle. Therefore, the intracycle interference can be written as

$$\mathbf{E}^{\text{hhg}}(\omega) = \mathbf{C}_1 + \mathbf{C}_2 e^{\Delta\varphi}, \quad \Delta\varphi = \omega\Delta t = \frac{\omega}{\omega_0} \pi. \quad (24)$$

\mathbf{C}_1 and \mathbf{C}_2 are vectors shown in Fig. 3(c). The phase difference $\Delta\varphi$ is derived from the half-cycle time delay. As shown

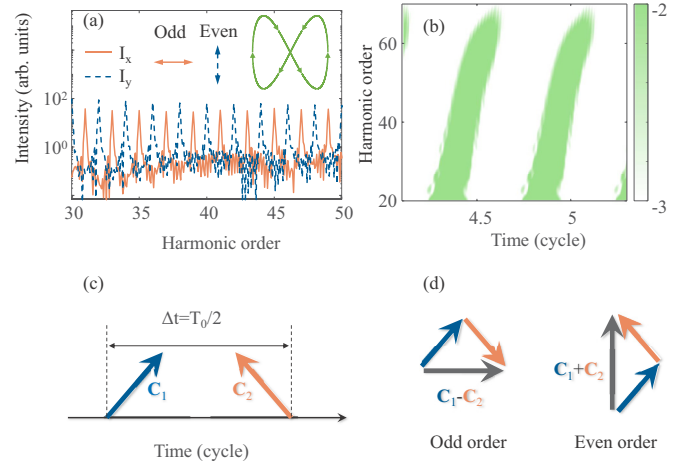


FIG. 3. The calculation results in the OTC field. The intensity of the fundamental and SH fields is 5×10^{14} W/cm². (a) The intensity of harmonic components parallel to the x and y directions. (b) The time-frequency spectrogram of the HHG. The color map represents the intensity distribution in the logarithmic scale. (c) The schematic diagram of intracycle interference. The two arrows show the amplitude, polarization angle, and emission time of two temporal components. (d) The interference results of odd- and even-order harmonics.

in Fig. 3(d), for odd-order harmonics, the phase difference is $(2n + 1)\pi$, which causes a sign reversion; therefore, the interference turns into $\mathbf{C}_1 - \mathbf{C}_2$. For even-order harmonics, the phase difference is $2n\pi$, and the interference is simplified as $\mathbf{C}_1 + \mathbf{C}_2$. Therefore, both odd- and even-order harmonics are linearly polarized, and their polarization directions are orthogonal.

B. Polarization of harmonics in nearly OTC driving fields

In this section, we investigate the origin of the ellipticity of harmonics in the nearly OTC field. The nearly OTC field can be written as

$$\mathbf{E}(t) = E_0 f(t) \begin{bmatrix} \cos(\omega_0 t) + \eta \cos \theta \cos(2\omega_0 t - \pi/2) \\ \eta \sin \theta \cos(2\omega_0 t - \pi/2) \end{bmatrix}, \quad (25)$$

where η and θ are the amplitude ratio and crossing angle between the SH and fundamental fields. As Fig. 4(a) shows, the Lissajous figure of the driving field is no longer symmetric about the y direction. The intensity distributions of right- and left-circularly polarized components are different in the spectrum, which leads to harmonics that are elliptically polarized. The Lissajous figures of H46 shows the ellipticity can reach 0.8, which is much larger than that in the OTC field. To explain the ellipticity, we investigate the time-frequency properties of the HHG process in Fig. 4(b). The cutoff energy of each channel is different from that in the OTC field shown in Fig. 3(b). Compared with those in Fig. 3(b), the cut-off energy of the former channel in Fig. 4(b) is lower, while the cut-off energy of latter channel is higher. The solid lines in Fig. 4(b) are calculated by representative paths, and the dashed lines show the corresponding results in the OTC field. It is obvious that the emission time of the harmonics also changes slightly. The time delay between two channels deviates from $0.5T_0$.

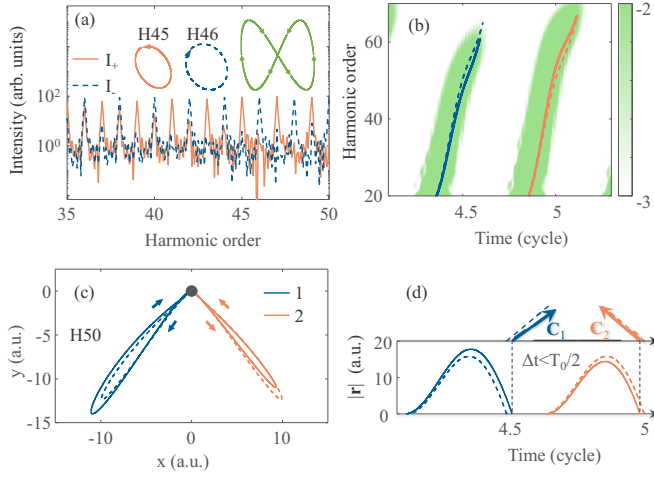


FIG. 4. The calculation result in nearly OTC field. The intensity of the fundamental and SH fields is 5×10^{14} W/cm²; their crossing angle is 85° . (a) The intensity of helical components of harmonics. (b) The time-frequency spectrogram of the HHG. The color map represents the intensity distribution in the logarithmic scale. The solid lines are obtained by path analysis. (c) The two representative electron paths. (d) The schematic diagram of intracycle interference. The two solid arrows show the amplitude, polarization angle, and emission time of two temporal components. The dashed lines in (b), (c), and (d) show the corresponding results in the OTC field as a reference.

This deviation can be explained by the dynamical asymmetry of quantum paths. Path 1 and path 2 shown in Fig. 4(c) are the representative quantum paths responsible for H50. The results indicate that electrons which recollide with parent ion during former half (4.2~4.7) optical cycle travel farther than electrons which recollide during latter half (4.7~5.2) optical cycle. Compared with those in the OTC field, the asymmetry of quantum paths affects the structure of the temporal interferometer. As Fig. 4(d) shows, vectors \mathbf{C}_1 and \mathbf{C}_2 are no longer symmetric about the y direction, and their time delay is shortened to $0.46T_0$. In addition, the dynamical phase difference ΔS leads to another phase difference. Therefore, the harmonics can be represented as

$$\mathbf{E}^{\text{hhg}}(\omega) = \mathbf{C}_1 + \mathbf{C}_2 e^{i(\Delta S - \omega \Delta t)}. \quad (26)$$

The right- and left-circularly polarized components can be written as

$$\mathbf{E}^{\text{hhg}}(\omega)_\pm \propto \begin{bmatrix} 1 \\ \mp i \end{bmatrix} \left\{ 1 + \frac{|\mathbf{C}_2|}{|\mathbf{C}_1|} \exp[i(\Delta\varphi \pm \Delta\alpha)] \right\}. \quad (27)$$

It is clear that the phase difference $\Delta\varphi$ and angle difference $\Delta\alpha$ determine the polarization of harmonics. If $\Delta\varphi = n\pi$, harmonics are linearly polarized, just like those in the OTC field. Otherwise, the harmonics are elliptically polarized. Particularly, if $\Delta\varphi \pm \Delta\alpha = (2n+1)\pi$, the right- and left-circularly polarized components interfere destructively, and the other helical component is dominant, which leads to a large ellipticity.

Next, we investigate the ellipticity features shown in Fig. 4(a). Like in Fig. 4(c), we show the representative quantum paths of different harmonics in Fig. 5. As harmonic order

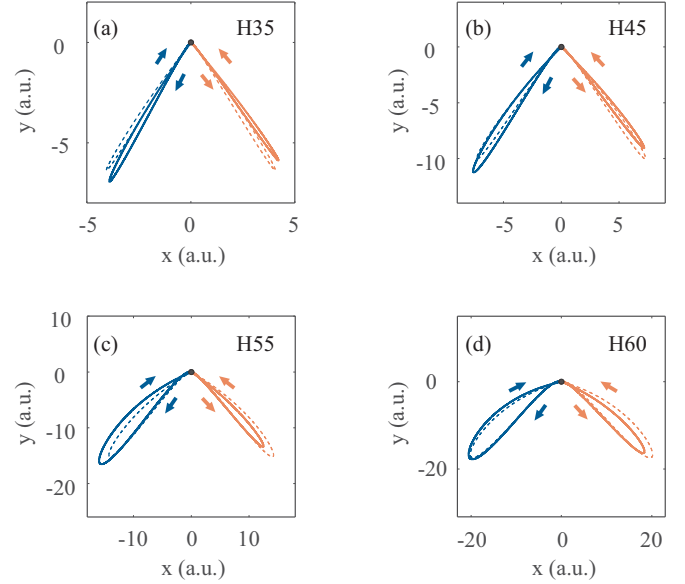


FIG. 5. Representative electron paths of different harmonics. The parameters are the same as those in Fig. 4.

increases, two properties become apparent: (i) For H35, the blue and orange solid paths have comparable lengths. As harmonic order increases to 55, the degree of asymmetry between the blue and orange solid paths increases. However, the difference in path length decreases as the harmonic order increases from 55 to 60. (ii) For H35, the solid paths locate on the right side of the dashed paths. As harmonic order increases, the solid paths move to the left side of the dashed path gradually. In Fig. 6(a), we show the dynamic phase ΔS and recollision time difference Δt between two representative paths. As harmonic order increases, both ΔS and Δt first decrease and then increase. As shown in Fig. 6(b), the total phase difference $\Delta\varphi = \Delta S - \omega\Delta t$ increases monotonously. Moreover, there is a π shift between adjacent even and odd harmonic orders. Figures 6(c) and 6(d) show the polarization angle θ^{hhg} (the angle of the major axis of the Lissajous figure) and the DCP ζ of each harmonic. As harmonic order increases, the ellipticity and polarization angle are modulated. When harmonic order is lower than 30, harmonics are nearly linearly polarized because $\Delta\varphi$ is close to $n\pi$. As harmonic order increases to 45, $\Delta\varphi$ increases obviously, and the ellipticity reaches the maximal value. As harmonic order increases further, $\Delta\varphi$ is close to $n\pi$ again; therefore, the DCP varies in the opposite direction.

In Fig. 7, we further investigate the influence of the crossing angle and intensity ratio on the harmonic polarization spectrum. For the sake of clarity, we present only the results for even-order harmonics. The analysis of odd-order harmonics is similar to that for the even ones. Figure 7(a1) shows the DCP is not monotonously related to the crossing angle. For harmonics higher than H40, the DCP varies between 1 and -1 alternately. The modulation of the ellipticity can also be explained by temporal interferometry. According to Eq. (27), the phase difference $\Delta\varphi$ plays an important role in determining the harmonic polarization. When adjusting the driving field, the quantum paths change, and $\Delta\varphi$ changes consequently.

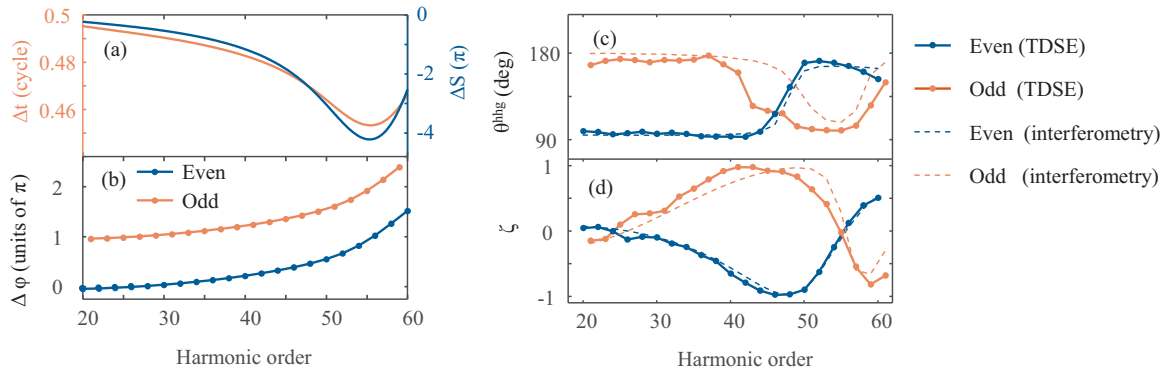


FIG. 6. The calculation results in nearly OTC field. The parameters are the same as those in Fig. 4. (a) and (b) show the time delay, action difference, and phase difference between two temporal components. (c) and (d) show the polarization angle and the degree of circular polarization of harmonics.

By analyzing the representative paths, we calculate $\Delta\varphi$ for different crossing angles, as shown in Fig. 7(a2). For each harmonic order, $\Delta\varphi$ increases monotonously with decreasing crossing angle. As shown in Fig. 7(a3), the DCP calculated by temporal double-slit interferometry is in good agreement with Fig. 7(a1). Similarly, the influence of the intensity ratio on ellipticity, shown in Fig. 7(b1), can also be explained as a modification of the temporal interferometer. Compared with Fig. 7(a2), the varying range of $\Delta\varphi$ in Fig. 7(b2) is smaller, which can be understood by the different influences of the crossing angle and intensity ratio in modulating the driving

laser field. When decreasing the crossing angle, the Lissajous figure of the driving field changes obviously, and the degree of asymmetry of the quantum paths increases continuously. However, when changing the intensity ratio, the Lissajous figure of the driving field is just stretched. Additionally, when the intensity ratio deviates from 1:1 too much, the synthesized driving field behaves like a one-color linearly polarized laser field; therefore, the degree of asymmetry of the quantum path decreases.

By using the interference model, one can realize optimal control over the harmonic ellipticity more conveniently. The

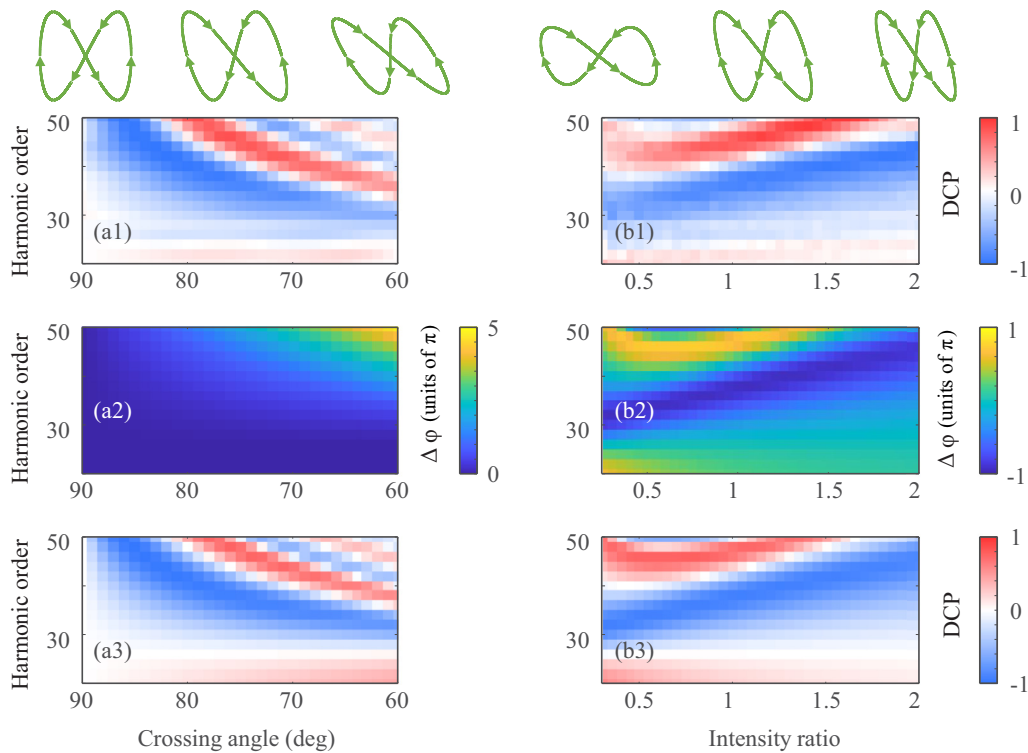


FIG. 7. The influence of crossing angle and intensity ratio on harmonics. Only even-order harmonics are presented. In (a), the intensity of the fundamental and SH fields is fixed at 5×10^{14} W/cm². In (b), the crossing angle between the fundamental field and the SH field is fixed at 75°. The intensity ratio is changed by adjusting the intensity of the SH field. The intensity of the fundamental field is fixed at 5×10^{14} W/cm². (a1) and (b1) The DCP calculated by TDSE. (a2) and (b2) The phase difference calculated by quantum path analysis. (a3) and (b3) The DCP calculated by temporal interferometry.

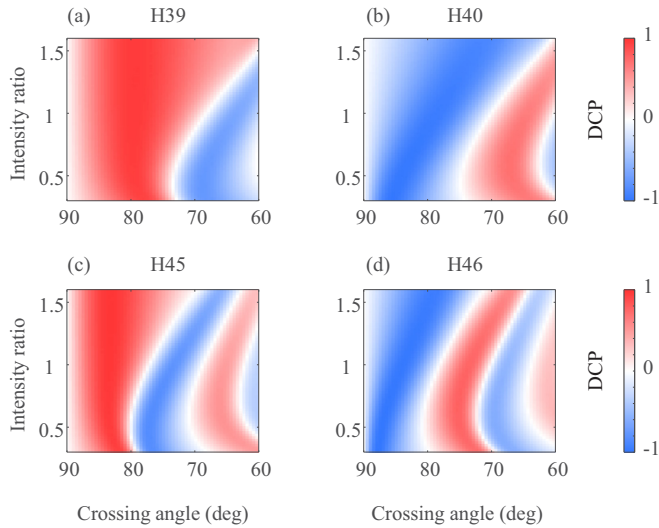


FIG. 8. The control of DCP of harmonics by modifying the nearly OTC field. The results are calculated by temporal interferometry.

DCPs of specific harmonics as a function of crossing angle and intensity ratio are shown in Fig. 8. The result shows that the magnitudes of the ellipticity of adjacent odd- and even-order harmonics are similar, but their signs are opposite. Meanwhile, as harmonic order increases, polarization is more sensitive to the driving fields. It is clear that by adjusting the crossing angle and intensity ratio, full control over polarization of the harmonic can be realized in nearly OTC fields.

To validate our results, we further perform calculations for the Ne atom with p symmetry in Fig. 9. The atomic Coulomb potential is modeled by the 2D effective potential $V(\mathbf{r}) = -[1 + 9 \exp(-\mathbf{r}^2)]/\sqrt{\mathbf{r}^2 + b}$. The parameters are the same as in [49]. The two degenerate current-carrying states $2p_{\pm}$ with magnetic quantum numbers $m = \pm 1$, denoted by $|\phi_{2p_{\pm}}\rangle$, are obtained as $|\phi_{2p_{\pm}}\rangle = (|\phi_{2p_x}\rangle \pm i|\phi_{2p_y}\rangle)/\sqrt{2}$, where $|\phi_{2p_x}\rangle$ and $|\phi_{2p_y}\rangle$ are obtained through imaginary-time propagation. We calculate the harmonic spectra from $|\phi_{2p_+}\rangle$ and $|\phi_{2p_-}\rangle$ by numerically solving TDSE and add up the two results coherently. As shown in Fig. 9, the polarization of harmonics from Ne is similar to that for He, shown in Fig. 6. The results of temporal interferometry are calculated by the reference $1s$ orbital with the same ionization potential of Ne. It is shown that our method can be applied to different noble gas atoms. For molecule targets, the plane wave approximation should be corrected, and the temporal interferometry model is still valid for resolving the polarization of high harmonics.

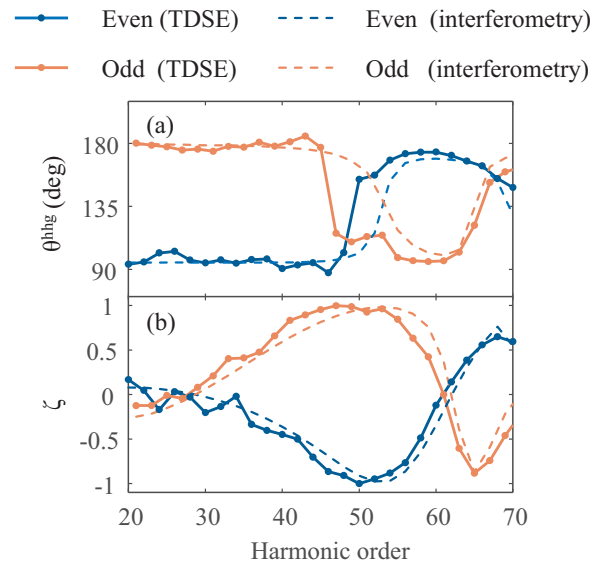


FIG. 9. The calculation results for $2p$ orbitals of the Ne atom. The wavelength of the fundamental field is 1000 nm. The intensity of the fundamental and SH fields is 3×10^{14} W/cm²; their crossing angle is 85° . (a) and (b) show the polarization angle and the degree of circular polarization of harmonics in nearly OTC field.

IV. CONCLUSION

In conclusion, we presented a temporal multislit interference model which can explain the polarization of high harmonics. We showed its applications in various driving fields. From the perspective of interference, the selection rules and ellipticity features of harmonics can be attributed to intracycle interference. Moreover, the control of polarization can be simply understood as the modulation of temporal interferometer. The results demonstrated that by adjusting the crossing angle and intensity ratio, full control over harmonic polarization can be realized in nearly orthogonal two-color fields. Our work shows the link between the harmonic polarization spectrum and the electron dynamics. It provides an intuitive and convenient method to investigate high-order harmonic generation. Meanwhile, the interference picture will facilitate the probe of electron dynamics from the harmonic spectrum.

ACKNOWLEDGMENT

This paper is supported by the National Natural Science Foundation of China (Grants No. 91950202, No. 11627809, No. 11874165, No. 11704137, No. 11934006, and No. 12021004).

[1] T. Popmintchev, M.-C. Chen, D. Popmintchev, P. Arpin, S. Brown, S. Ališauskas, G. Andriukaitis, T. Balčiunas, O. Mücke, A. Pugzlys, A. Baltuška, B. Shim, S. Schrauth, A. Gaeta, C. Hernández-García, L. Plaja, A. Becker, A. Jaron-Becker, M. Murnane, and H. Kapteyn, *Science* **336**, 1287 (2012).

[2] E. Takahashi, P. Lan, O. Mücke, Y. Nabekawa, and K. Midorikawa, *Nat. Commun.* **4**, 2691 (2013).

[3] Y. Mairesse, A. de Bohan, L. J. Frasinski, H. Merdji, L. C. Dinu, P. Monchicourt, P. Breger, M. Kovačev, R. Taïeb, B. Carré, H. G. Muller, P. Agostini, and P. Salières, *Science* **302**, 1540 (2003).

- [4] C. Zhai, X. Zhang, X. Zhu, L. He, Y. Zhang, B. Wang, Q. Zhang, P. Lan, and P. Lu, *Opt. Express* **26**, 2775 (2018).
- [5] J. Itatani, J. Lavesque, D. Zeidler, H. Niikura, H. Pépin, J. Kieffer, P. Corkum, and D. Villeneuve, *Nature (London)* **432**, 867 (2004).
- [6] H. Niikura, N. Dudovich, D. M. Villeneuve, and P. B. Corkum, *Phys. Rev. Lett.* **105**, 053003 (2010).
- [7] L. Li, P. Lan, L. He, W. Cao, Q. Zhang, and P. Lu, *Phys. Rev. Lett.* **124**, 157403 (2020).
- [8] P. B. Corkum, *Phys. Rev. Lett.* **71**, 1994 (1993).
- [9] K. J. Schafer, B. Yang, L. F. DiMauro, and K. C. Kulander, *Phys. Rev. Lett.* **70**, 1599 (1993).
- [10] L. Li, P. Lan, X. Zhu, T. Huang, Q. Zhang, M. Lein, and P. Lu, *Phys. Rev. Lett.* **122**, 193901 (2019).
- [11] N. Böwering, T. Lischke, B. Schmidtke, N. Müller, T. Khalil, and U. Heinzmann, *Phys. Rev. Lett.* **86**, 1187 (2001).
- [12] O. Travnikova, J.-C. Liu, A. Lindblad, C. Nicolas, J. Söderström, V. Kimberg, F. Gel'mukhanov, and C. Miron, *Phys. Rev. Lett.* **105**, 233001 (2010).
- [13] J. Stöhr, Y. Wu, B. D. Hermsmeier, M. G. Samant, G. R. Harp, S. Koranda, D. Dunham, and B. P. Tonner, *Science* **259**, 658 (1993).
- [14] N. Sun, X. Zhu, B. Wang, D. Wang, R. Shao, P. Lan, and P. Lu, *Phys. Rev. A* **101**, 053437 (2020).
- [15] K. M. Dorney, J. L. Ellis, C. Hernández-García, D. D. Hickstein, C. A. Mancuso, N. Brooks, T. Fan, G. Fan, D. Zusin, C. Gentry, P. Grychtol, H. C. Kapteyn, and M. M. Murnane, *Phys. Rev. Lett.* **119**, 063201 (2017).
- [16] R. Shao, C. Zhai, Y. Zhang, N. Sun, W. Cao, P. Lan, and P. Lu, *Opt. Express* **28**, 15874 (2020).
- [17] L. Medišauskas, J. Wragg, H. van der Hart, and M. Y. Ivanov, *Phys. Rev. Lett.* **115**, 153001 (2015).
- [18] N. Zhavoronkov and M. Ivanov, *Opt. Lett.* **42**, 4720 (2017).
- [19] P.-C. Huang, C. Hernández-García, J.-T. Huang, P.-Y. Huang, C.-H. Lu, L. Rego, D. Hickstein, J. Ellis, A. Jaron-Becker, A. Becker, S.-D. Yang, C. Durfee, L. Plaja, H. Kapteyn, M. Murnane, A. Kung, and M.-C. Chen, *Nat. Photonics* **12**, 349 (2018).
- [20] C. Zhai, X. Zhu, J. Long, R. Shao, Y. Zhang, L. He, Q. Tang, Y. Li, P. Lan, B. Yu, and P. Lu, *Phys. Rev. A* **103**, 033114 (2021).
- [21] X. Zhou, R. Lock, N. Wagner, W. Li, H. C. Kapteyn, and M. M. Murnane, *Phys. Rev. Lett.* **102**, 073902 (2009).
- [22] Y. Mairesse, J. Higuët, N. Dudovich, D. Shafir, B. Fabre, E. Mével, E. Constant, S. Patchkovskii, Z. Walters, M. Y. Ivanov, and O. Smirnova, *Phys. Rev. Lett.* **104**, 213601 (2010).
- [23] F. A. Weihe, S. K. Dutta, G. Korn, D. Du, P. H. Bucksbaum, and P. L. Shkolnikov, *Phys. Rev. A* **51**, R3433(R) (1995).
- [24] P. Antoine, A. L'Huillier, M. Lewenstein, P. Salières, and B. Carré, *Phys. Rev. A* **53**, 1725 (1996).
- [25] V. V. Strelkov, A. A. Gonoskov, I. A. Gonoskov, and M. Y. Ryabikin, *Phys. Rev. Lett.* **107**, 043902 (2011).
- [26] O. Kfir, P. Grychtol, E. Turgut, R. Knut, D. Zusin, D. Popmintchev, T. Popmintchev, H. Nembach, J. Shaw, A. Fleischer, H. Kapteyn, M. Murnane, and O. Cohen, *Nat. Photonics* **9**, 99 (2015).
- [27] T. Fan *et al.*, *Proc. Natl. Acad. Sci. USA* **112**, 14206 (2015).
- [28] A. Fleischer, O. Kfir, T. Diskin, P. Sidorenko, and O. Cohen, *Nat. Photonics* **8**, 543 (2014).
- [29] X. Liu, X. Zhu, L. Li, Y. Li, Q. Zhang, P. Lan, and P. Lu, *Phys. Rev. A* **94**, 033410 (2016).
- [30] G. Lambert, B. Vodungbo, J. Gautier, B. Mahieu, V. Malka, S. Sebban, P. Zeitoun, J. Luning, J. Perron, A. Andreev, S. Stremoukhov, F. Ardana-Lamas, A. Dax, C. Hauri, A. Sardinha, and M. Fajardo, *Nat. Commun.* **6**, 6167 (2015).
- [31] S. Stremoukhov, A. Andreev, B. Vodungbo, P. Salières, B. Mahieu, and G. Lambert, *Phys. Rev. A* **94**, 013855 (2016).
- [32] B. Mahieu, S. Stremoukhov, D. Gauthier, C. Spezzani, C. Alves, B. Vodungbo, P. Zeitoun, V. Malka, G. De Ninno, and G. Lambert, *Phys. Rev. A* **97**, 043857 (2018).
- [33] C. Zhai, R. Shao, P. Lan, B. Wang, Y. Zhang, H. Yuan, S. M. Njoroge, L. He, and P. Lu, *Phys. Rev. A* **101**, 053407 (2020).
- [34] Y. Fang and Y. Liu, *Phys. Rev. A* **103**, 033116 (2021).
- [35] D. Shafir, Y. Mairesse, H. Wörner, K. Rupnik, D. Villeneuve, P. Corkum, and N. Dudovich, *New J. Phys.* **12**, 073032 (2010).
- [36] O. Neufeld, D. Podolsky, and O. Cohen, *Nat. Commun.* **10**, 405 (2019).
- [37] O. E. Alon, V. Averbukh, and N. Moiseyev, *Phys. Rev. Lett.* **80**, 3743 (1998).
- [38] E. Pisanty, S. Sukiasyan, and M. Ivanov, *Phys. Rev. A* **90**, 043829 (2014).
- [39] M. Feit, J. Fleck, and A. Steiger, *J. Comput. Phys.* **47**, 412 (1982).
- [40] X. Zhang, L. Li, X. Zhu, X. Liu, Q. Zhang, P. Lan, and P. Lu, *Phys. Rev. A* **94**, 053408 (2016).
- [41] D. B. Milošević, W. Becker, and R. Kopold, *Phys. Rev. A* **61**, 063403 (2000).
- [42] P. Salières, B. Carré, L. Le Déroff, F. Grasbon, G. Paulus, H. Walther, R. Kopold, W. Becker, D. Milošević, A. Sanpera, and M. Lewenstein, *Science* **292**, 902 (2001).
- [43] D. Shafir, H. Soifer, B. Bruner, M. Dagan, Y. Mairesse, S. Patchkovskii, M. Ivanov, O. Smirnova, and N. Dudovich, *Nature (London)* **485**, 343 (2012).
- [44] P. Paul, E. Toma, P. Breger, G. Mullot, F. Augé, P. Balcou, H. Muller, and P. Agostini, *Science* **292**, 1689 (2001).
- [45] P. Antoine, A. L'Huillier, and M. Lewenstein, *Phys. Rev. Lett.* **77**, 1234 (1996).
- [46] G. F. Gribakin and M. Y. Kuchiev, *Phys. Rev. A* **55**, 3760 (1997).
- [47] E. Pisanty, M. Ciappina, and M. Lewenstein, *J. Phys. Photonics* **2**, 034013 (2020).
- [48] C. C. Chirilă, I. Dreisigacker, E. V. van der Zwan, and M. Lein, *Phys. Rev. A* **81**, 033412 (2010).
- [49] X. Zhang, X. Zhu, X. Liu, F. Wang, M. Qin, Q. Liao, and P. Lu, *Phys. Rev. A* **102**, 033103 (2020).